

Heavy neutral leptons and top quarks in effective field theory

Rebeca Beltrán,^a Giovanna Cottin,^{b,c} Julian Günther,^d Martin Hirsch,^a Arsenii Titov,^e Zeren Simon Wang^{f,g}

^a*AHEP Group, Instituto de Física Corpuscular – CSIC/Universitat de València, Apartado 22085, E-46071 València, Spain*

^b*Instituto de Física, Pontificia Universidad Católica de Chile, Avenida Vicuña Mackenna 4860, Santiago, Chile*

^c*Millennium Institute for Subatomic Physics at the High Energy Frontier (SAPHIR), Fernández Concha 700, Santiago, Chile*

^d*Bethe Center for Theoretical Physics & Physikalisches Institut der Universität Bonn, Nußallee 12, 53115 Bonn, Germany*

^e*Dipartimento di Fisica “Enrico Fermi”, Università di Pisa and INFN, Sezione di Pisa, Largo Bruno Pontecorvo 3, I-56127 Pisa, Italy*

^f*Department of Physics, National Tsing Hua University, Hsinchu 300, Taiwan*

^g*Center for Theory and Computation, National Tsing Hua University, Hsinchu 300, Taiwan*

*E-mail: rebeca.beltran@ific.uv.es, gfcottin@uc.cl,
guenther@physik.uni-bonn.de, mahirsch@ific.uv.es,
arsenii.titov@df.unipi.it, wzs@mx.nthu.edu.tw*

ABSTRACT: We study the phenomenology of heavy neutral leptons (HNLs) at the LHC in effective field theory, concentrating on $d = 6$ operators with top quarks. Depending on the operator choice and HNL mass, the HNLs will be produced either from proton-proton collisions in association with a single top, or via non-standard decays of top quarks. For long-lived HNLs we estimate the sensitivity reach of different detectors to various operators with top quarks and the HNLs for the high-luminosity phase of the LHC. For certain operators, ATLAS and some far detectors (MATHUSLA and ANUBIS) will be able to probe the associated new-physics scale as large as 12 TeV and 4.5 TeV, respectively, covering complementary HNL-mass ranges.

Contents

1	Introduction	1
2	Effective operators and benchmark scenarios	3
2.1	HNL production	3
2.2	HNL decays	7
2.3	Benchmark scenarios	10
3	Experiments and simulation	11
3.1	ATLAS	11
3.2	Far detectors	14
4	Numerical results	16
5	Conclusions	20

1 Introduction

The long-lived-particle (LLP) programs at the LHC have gained considerable momentum in the past few years [1–4]. Among the many proposals for the LLPs, one of the simplest and best motivated candidates are heavy neutral leptons (HNLs). In minimal models, the HNLs are characterized solely by their mass and three mixing parameters (per HNL generation). Such minimal HNLs have been searched for in many experiments. For a recent summary of bounds, see *e.g.* Refs. [5, 6]. At the LHC, HNLs can be constrained particularly strongly using displaced searches, and sensitivity projections for the LHC in the high-luminosity phase can be found in Refs. [7–11].

New physics, however, may not be limited to a minimal HNL. A number of UV-complete models have been discussed in the literature where the HNLs have non-minimal interactions that greatly change the expectations for HNL production (and decay) at the LHC. Examples of such models include Z' models [12, 13], models with additional scalars [14, 15], and leptoquark models [16, 17].

However, in the absence of any new resonances at the LHC, effective field theory (EFT) is probably the best tool of choice. N_R -extended Standard Model effective field theory (N_R SMEFT) is the EFT that describes the Standard Model (SM) with additional (n copies) of a light fermionic singlet [18–23].¹ A complete classification of mass dimension $d \leq 7$ operators containing N_R can be found in Ref. [20], and that of $d \leq 9$ operators in

¹Sometimes this is also called ν SMEFT in the literature. We prefer N_R SMEFT to stress the (mostly) singlet character of the fermion and avoid confusions with the SM neutrinos.

Ref. [24], while a list of possible tree-level completions for N_R SMEFT operators of $d \leq 7$ is given in Ref. [25].

A number of papers have studied the phenomenology of HNLs in the N_R SMEFT (or its low-energy variant N_R -extended low-energy EFT, N_R LEFT [26–29]) recently. For instance, τ -lepton decays to sterile neutrinos in the EFT at Belle II were studied in Ref. [30]. The HNL production via $d = 5$ operators in Higgs decays was considered in Refs. [31–35] and via $d = 5$ and $d = 6$ operators in Ref. [36]. Considering the HNLs produced in decays of mesons that will be copiously produced at the high-luminosity LHC, the sensitivity to $d = 6$ N_R operators with charged leptons was calculated in Ref. [37] and that to N_R operators with active neutrinos was obtained in Ref. [38]. At the LHC, the HNLs in the N_R SMEFT can be produced also directly from parton (quark) collisions. For this case, operators with pairs of N_R 's have been studied in Ref. [39], while for operators that produce a single N_R , see Ref. [40]. We also mention Refs. [41, 42], which derive limits on various EFT operators with N_R 's from reinterpretation of previous HNL searches. Moreover, a set of dipole operators coupling the HNLs to the SM gauge bosons can lead to displaced decays of the HNL into a photon and a neutrino, and this scenario has been studied for several collider experiments [43–49]. Further studies investigated the phenomenology of some of the N_R SMEFT operators at future lepton [50, 51] and lepton-hadron [52–54] colliders (see also Refs. [55, 56]).

None of the above papers, however, considered operators with top quarks. N_R 's produced from non-standard decays of the top quarks were studied in Ref. [57], for the particular case of collider-stable (massless or nearly massless) N_R . Since for a stable N_R the final state of the top quark decay is very similar to that in the SM, the background is rather large and the limits that could potentially be obtained are quite weak: Ref. [57] estimates a limit on the scale $\Lambda \geq 0.33$ TeV for an integrated luminosity of $\mathcal{L} = 3$ ab $^{-1}$. Recently, Ref. [58] discussed production and decay rates of (long-lived) SM singlets including N_R , induced by four-fermion operators involving the top quark. However, no detector simulations were performed therein.

In this paper, we will study long-lived HNLs produced in the framework of the N_R SMEFT either from direct production in association with a top quark, or from top quark decays. The HNL is assumed to be long-lived enough to either produce a displaced signal in the ATLAS or CMS detector, or even lead to signal events in one of the proposed “far” detectors including MATHUSLA [59] and ANUBIS [60]. The phenomenology depends on the operator type under consideration. We distinguish pair and singly produced N_R . For pair- N_R operators, the N_R can decay only via active-sterile-neutrino mixing, whereas for operators with a single N_R both production and decay can be induced by the same operator. In the latter case, it then depends strongly on the mass of the HNL, to determine whether the N_R decay is dominated by the mixing or the operator. Different from Ref. [57], the displaced vertex from the N_R decay can be used to reduce backgrounds. Thus, the sensitivity to N_R SMEFT operator scales is greatly improved. We estimate that with $\mathcal{L} = 3$ ab $^{-1}$ of integrated luminosity, scales up to $\Lambda \simeq 12$ (4.5) TeV could be probed by ATLAS

(MATHUSLA and ANUBIS).²

The rest of this paper is organized as follows. In section 2, we define the $d = 6$ operators that we choose to study and discuss the production and decay modes of the HNL associated to these operators. In section 3, we provide a brief summary of the experiments that we will consider and the detail of the numerical simulation. In section 4, we present and discuss the sensitivity results. We summarize our findings and conclude in section 5.

2 Effective operators and benchmark scenarios

We assume the existence of (i) a right-handed neutrino N_R with mass m_N below or around the weak scale $v = 246$ GeV, and (ii) heavy new states at the scale $\Lambda \gg v$ that mediate interactions between N_R and the top quark t . At the energies much smaller than Λ , such interactions can be parameterized by higher-dimensional operators involving N_R and t , which are invariant under the SM gauge symmetry; see *e.g.* Ref. [57]. In this work, we focus on the lepton- and baryon-number-conserving four-fermion operators with these fields. We assume one generation of N_R and, for simplicity, consider the first and third generations of the SM quarks, and the first generation of SM leptons. The interactions of interest can be divided into pair- N_R and single- N_R operators and are shown in table 1. Here, $Q_i = (u_{iL}, d_{iL})^T$ and $L = (\nu_L, e_L)^T$ denote the $SU(2)_L$ doublets, and ϵ is the Levi-Civita symbol in two dimensions. We note that the operator

$$\begin{aligned} \mathcal{O}_{LdQN}^{i3} &= (\bar{L}d_{iR}) \epsilon \left(\bar{Q}_3^T N_R \right) = (\bar{\nu}_L d_{iR}) (\bar{b}_L N_R) - (\bar{e}_L d_{iR}) (\bar{t}_L N_R) \\ &= -\frac{1}{2} \mathcal{O}_{LNQd}^{3i} - \frac{1}{8} [(\bar{\nu}_L \sigma^{\mu\nu} N_R) (\bar{b}_L \sigma_{\mu\nu} d_{iR}) - (\bar{e}_L \sigma^{\mu\nu} N_R) (\bar{t}_L \sigma_{\mu\nu} d_{iR})], \end{aligned}$$

where $\sigma^{\mu\nu} = i[\gamma^\mu, \gamma^\nu]/2$, has the same particle content as \mathcal{O}_{LNQd}^{3i} , but includes a different Lorentz structure.

2.1 HNL production

Pair- N_R operators. The pair- N_R interactions \mathcal{O}_{uN}^{13} and \mathcal{O}_{QN}^{13} induce the flavor-violating rare top decay $t \rightarrow uN\bar{N}$. The corresponding decay width is given by [57]³

$$\Gamma(t \rightarrow uN\bar{N}) = \frac{m_t^5 g(x)}{1536\pi^3 \Lambda^4} \left[(c_{uN}^{13})^2 + (c_{QN}^{13})^2 \right], \quad (2.1)$$

where

$$\begin{aligned} g(x) &= (1 - 14x - 2x^2 - 12x^3) \sqrt{1 - 4x} \\ &\quad - 12x^2 (1 - x^2) \left[\ln \frac{1 - \sqrt{1 - 4x}}{1 + \sqrt{1 - 4x}} - \ln \frac{1 + \sqrt{1 - 4x} - 2x}{2x} \right], \end{aligned} \quad (2.2)$$

²We note that while in the present work we will focus on direct limits that could be set at the HL-LHC, it would also be interesting to study indirect effects of the top- N_R operators and derive associated bounds, similarly to what has been done for the top operators in the SMEFT [61].

³In Ref. [57], m_N is assumed to be negligibly small. In what follows, we keep track of it, since we are interested in a broad range of the HNL masses.

	Name	Structure (+ h.c. when needed)
Pair- N_R	\mathcal{O}_{uN}^{13}	$(\overline{\mathbf{u}_R}\gamma^\mu\mathbf{t}_R)(\overline{\mathbf{N}_R}\gamma_\mu\mathbf{N}_R)$
	\mathcal{O}_{uN}^{33}	$(\overline{\mathbf{t}_R}\gamma^\mu\mathbf{t}_R)(\overline{\mathbf{N}_R}\gamma_\mu\mathbf{N}_R)$
	\mathcal{O}_{QN}^{13}	$(\overline{\mathbf{Q}_1}\gamma^\mu\mathbf{Q}_3)(\overline{\mathbf{N}_R}\gamma_\mu\mathbf{N}_R) = (\overline{\mathbf{u}_L}\gamma^\mu\mathbf{t}_L)(\overline{\mathbf{N}_R}\gamma_\mu\mathbf{N}_R) + (\overline{\mathbf{d}_L}\gamma^\mu\mathbf{b}_L)(\overline{\mathbf{N}_R}\gamma_\mu\mathbf{N}_R)$
	\mathcal{O}_{QN}^{33}	$(\overline{\mathbf{Q}_3}\gamma^\mu\mathbf{Q}_3)(\overline{\mathbf{N}_R}\gamma_\mu\mathbf{N}_R) = (\overline{\mathbf{t}_L}\gamma^\mu\mathbf{t}_L)(\overline{\mathbf{N}_R}\gamma_\mu\mathbf{N}_R) + (\overline{\mathbf{b}_L}\gamma^\mu\mathbf{b}_L)(\overline{\mathbf{N}_R}\gamma_\mu\mathbf{N}_R)$
Single- N_R	\mathcal{O}_{duNe}^{13}	$(\overline{\mathbf{d}_R}\gamma^\mu\mathbf{t}_R)(\overline{\mathbf{N}_R}\gamma_\mu\mathbf{e}_R)$
	\mathcal{O}_{duNe}^{33}	$(\overline{\mathbf{b}_R}\gamma^\mu\mathbf{t}_R)(\overline{\mathbf{N}_R}\gamma_\mu\mathbf{e}_R)$
	\mathcal{O}_{LNQd}^{31}	$(\overline{\mathbf{L}}N_R)\epsilon(\overline{\mathbf{Q}_3}^T d_R) = (\overline{\nu_L}N_R)(\overline{\mathbf{b}_L}d_R) - (\overline{\mathbf{e}_L}N_R)(\overline{\mathbf{t}_L}d_R)$
	\mathcal{O}_{LNQd}^{33}	$(\overline{\mathbf{L}}N_R)\epsilon(\overline{\mathbf{Q}_3}^T b_R) = (\overline{\nu_L}N_R)(\overline{\mathbf{b}_L}b_R) - (\overline{\mathbf{e}_L}N_R)(\overline{\mathbf{t}_L}b_R)$
	\mathcal{O}_{LdQN}^{13}	$(\overline{\mathbf{L}}d_R)\epsilon(\overline{\mathbf{Q}_3}^T N_R) = (\overline{\nu_L}d_R)(\overline{\mathbf{b}_L}N_R) - (\overline{\mathbf{e}_L}d_R)(\overline{\mathbf{t}_L}N_R)$
	\mathcal{O}_{LdQN}^{33}	$(\overline{\mathbf{L}}b_R)\epsilon(\overline{\mathbf{Q}_3}^T N_R) = (\overline{\nu_L}b_R)(\overline{\mathbf{b}_L}N_R) - (\overline{\mathbf{e}_L}b_R)(\overline{\mathbf{t}_L}N_R)$
	\mathcal{O}_{QuNL}^{13}	$(\overline{\mathbf{Q}_1}t_R)(\overline{\mathbf{N}_R}L) = (\overline{\mathbf{u}_L}t_R)(\overline{\mathbf{N}_R}\nu_L) + (\overline{\mathbf{d}_L}t_R)(\overline{\mathbf{N}_R}e_L)$
	\mathcal{O}_{QuNL}^{31}	$(\overline{\mathbf{Q}_3}u_R)(\overline{\mathbf{N}_R}L) = (\overline{\mathbf{t}_L}u_R)(\overline{\mathbf{N}_R}\nu_L) + (\overline{\mathbf{b}_L}u_R)(\overline{\mathbf{N}_R}e_L)$
\mathcal{O}_{QuNL}^{33}	$(\overline{\mathbf{Q}_3}t_R)(\overline{\mathbf{N}_R}L) = (\overline{\mathbf{t}_L}t_R)(\overline{\mathbf{N}_R}\nu_L) + (\overline{\mathbf{b}_L}t_R)(\overline{\mathbf{N}_R}e_L)$	

Table 1. Lepton- and baryon-number-conserving four-fermion pair- N_R and single- N_R operators with the top quark. The indices label the quark generations. We focus on the first and third quark generations. The terms in boldface are relevant for the HNL production and/or decay associated with one top quark.

and $x = m_N^2/m_t^2$. At the same time, these operators mediate the direct production of an $N\bar{N}$ -pair in association with a top quark (as well as with a bottom quark for \mathcal{O}_{QN}^{13}) in pp collisions at the LHC, through the diagrams shown in figure 1.

At the LHC, top quarks are dominantly produced in pair through the strong interaction. The inclusive cross-section of $t\bar{t}$ production at the LHC with $\sqrt{s} = 13$ TeV is $\sigma_{t\bar{t}} = 830 \pm 38$ pb [62]. The single-top production through the weak interaction has a smaller cross-section: $\sigma_{tq+\bar{t}q} = 221 \pm 13$ pb at $\sqrt{s} = 13$ TeV [63]. In what follows, when considering the SM production of the top quark, we will focus on the top quark pair production.

To give an example of the relative importance of the two HNL production mechanisms introduced above, we simulate with `MadGraph5` [64, 65] (i) $pp \rightarrow t\bar{t}$ with a subsequent rare top decay $t \rightarrow uN\bar{N}$, (ii) $pp \rightarrow tN\bar{N}$, and (iii) $pp \rightarrow \bar{t}N\bar{N}$ induced by the operator \mathcal{O}_{uN}^{13} . The resulting cross-sections obtained for $\Lambda = 1$ TeV and $\sqrt{s} = 14$ TeV are shown in the upper-left panel of figure 2. The individual production modes are identified by

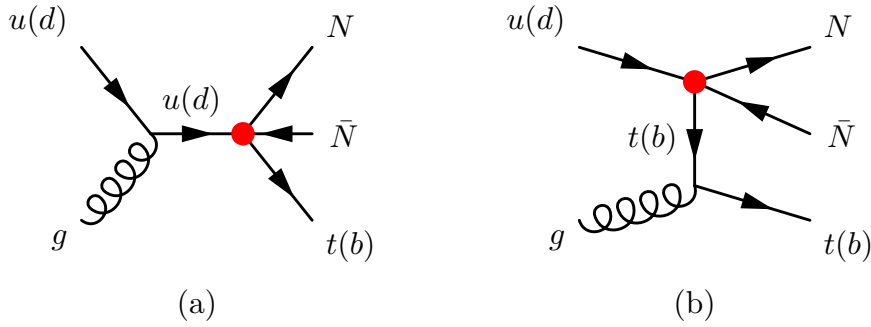


Figure 1. Production of an $N\bar{N}$ -pair in association with a t -quark (t - or b -quark) through \mathcal{O}_{uN}^{13} (\mathcal{O}_{QN}^{13}) denoted by the red blob. (The diagrams with the particles in parentheses are present for \mathcal{O}_{QN}^{13} , but not for \mathcal{O}_{uN}^{13} .)

labels in the plots. We observe that $\sigma(pp \rightarrow tN\bar{N})$ and $\sigma(pp \rightarrow \bar{t}N\bar{N})$ dominate over $\sigma(pp \rightarrow t\bar{t})[\mathcal{B}(t \rightarrow uN\bar{N}) + \mathcal{B}(\bar{t} \rightarrow \bar{u}N\bar{N})]$ in the whole range of HNL masses of interest, where \mathcal{B} denotes decay branching ratio.⁴ The main difference between the shape of the cross-sections for these two production modes is the behavior at larger m_N values. The contribution from top decays is highly suppressed when m_N approaches $m_t/2$, whereas in direct pp collisions the cross-section remains relatively flat up to a few hundreds of GeV. The difference in the cross-sections for $pp \rightarrow tN\bar{N}$ and $pp \rightarrow \bar{t}N\bar{N}$ is due to the larger parton distribution function (PDF) of the u -quark compared to that of \bar{u} inside the proton. We note that the production cross-sections for the states $tN\bar{N}/\bar{t}N\bar{N}$ from operator \mathcal{O}_{QN}^{13} are identical to the ones shown for \mathcal{O}_{uN}^{13} . We therefore do not show plots for this case.

The operators \mathcal{O}_{uN}^{33} and \mathcal{O}_{QN}^{33} neither trigger a top decay, nor do they contribute to the direct HNL production in pp collisions. Therefore, we will not consider them in what follows.

Single- N_R operators. The operators with off-diagonal quark-flavor indices, *viz.* 13 and 31, trigger the flavor-violating decays $t \rightarrow de^+N$ and $t \rightarrow u\bar{\nu}N/u\nu\bar{N}$ with the following widths: [57]

$$\Gamma(t \rightarrow de^+N) = \frac{m_t^5 f(x)}{6144\pi^3 \Lambda^4} \left[4(c_{duNe}^{13})^2 + (c_{QuNL}^{13})^2 + (c_{LNQd}^{31})^2 + (c_{LdQN}^{13})^2 - c_{LNQd}^{31}c_{LdQN}^{13} \right], \quad (2.3)$$

$$\Gamma(t \rightarrow u\bar{\nu}N) = \frac{m_t^5 f(x)}{6144\pi^3 \Lambda^4} (c_{QuNL}^{13})^2 \quad \text{and} \quad \Gamma(t \rightarrow u\nu\bar{N}) = \frac{m_t^5 f(x)}{6144\pi^3 \Lambda^4} (c_{QuNL}^{31})^2, \quad (2.4)$$

where $f(x) = 1 - 8x + 8x^3 - x^4 - 12x^2 \ln x$, and $x = m_N^2/m_t^2$. The same operators also contribute to the single-top production in association with either a charged lepton and an

⁴We generate events at leading order and multiply only the top-antitop quark production cross-section by a flat factor of $k \sim 1.7$ corresponding to the cross-section determined at NNLO+NNLL by the `Top++2.0` program [66]. We do not introduce correction factors for HNL production rate in direct pp collisions.

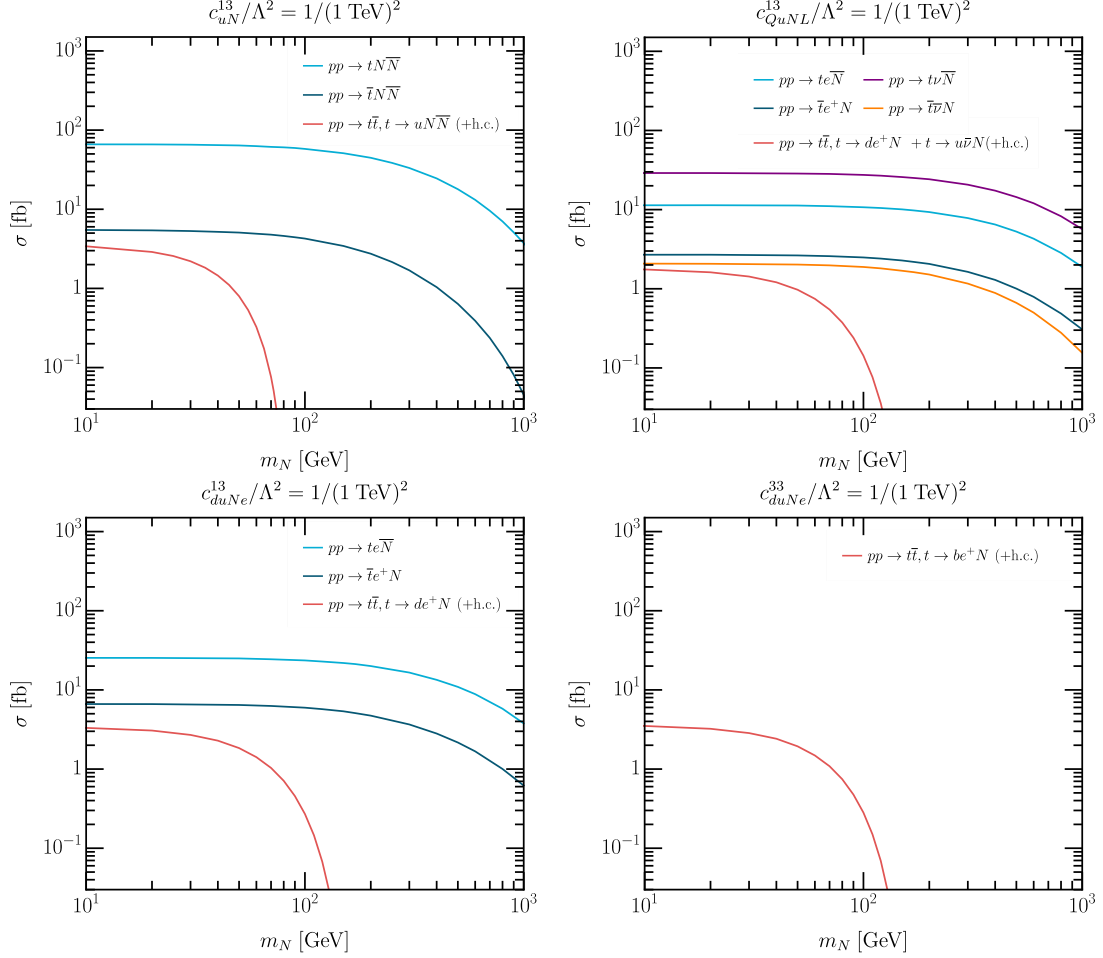


Figure 2. HNL production cross-sections induced by the operators \mathcal{O}_{uN}^{13} (top left), \mathcal{O}_{QuNL}^{13} (top right), \mathcal{O}_{duNe}^{13} (bottom left), \mathcal{O}_{duNe}^{33} (bottom right), for $c_{\mathcal{O}}^{ij} = 1$ and $\Lambda = 1$ TeV at the LHC with $\sqrt{s} = 14$ TeV.

HNL, or an SM neutrino and an HNL, directly in pp collisions.

The operators with $Q_3 = (t_L, b_L)^T$, *i.e.* \mathcal{O}_{LNQd}^{31} , \mathcal{O}_{LdQN}^{13} , and \mathcal{O}_{QuNL}^{31} , in addition give a contribution to the single-bottom production in association with either $\nu\bar{N}$ or e^+N .

As an example, we show in figure 3 the diagrams for the processes triggered by \mathcal{O}_{duNe}^{13} and \mathcal{O}_{LNQd}^{31} .

In the lower-left panel of figure 2, we display the cross-sections for (i) $pp \rightarrow t\bar{t}$ followed by a subsequent decay $t \rightarrow de^+N$, (ii) $pp \rightarrow te^-\bar{N}$, and (iii) $pp \rightarrow \bar{t}e^+N$, triggered by \mathcal{O}_{duNe}^{13} , setting $\Lambda = 1$ TeV. As in the case of the pair- N_R operator \mathcal{O}_{uN}^{13} , the direct HNL production in pp collisions dominates over the production through the new top quark decay. Compared to \mathcal{O}_{uN}^{13} , the cross-section for $pp \rightarrow te^-\bar{N}$ is smaller than that for $pp \rightarrow tN\bar{N}$, which is due to a smaller PDF of the d -quark with respect to the one of the u -quark.

In the upper-right panel of figure 2, we show the cross-sections for the processes induced by \mathcal{O}_{QuNL}^{13} . Since this operator involves $SU(2)_L$ doublets Q_1 and L , we have both $te\bar{N}$ and

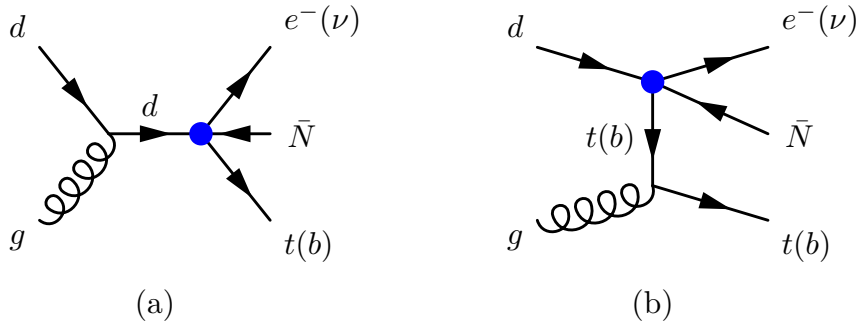


Figure 3. HNL production in association with e^- and t (e^- and t or ν and b) through \mathcal{O}_{duNe}^{13} (\mathcal{O}_{LNQd}^{31}) denoted by the blue blob. The diagrams with the particles in parentheses are present for \mathcal{O}_{LNQd}^{31} , but not for \mathcal{O}_{duNe}^{13} .

$t\nu\bar{N}$ final states (as well as their charge conjugates). As in the previous cases, the direct HNL production in pp collisions dominates over the production through new top quark decays.

The operators with the 33 quark-flavor indices lead to the flavor-conserving decay $t \rightarrow be^+N$ for which the width can be computed by eq. (2.3) with all quark-flavor indices set to 33. The contribution of these flavor-diagonal operators to the single-top and single-bottom production (in association with an electron or neutrino and an HNL) is negligible because of the smallness of the b -quark PDF. As an example, we show in the lower-right panel of figure 2 the only HNL production process that is induced by \mathcal{O}_{duNe}^{33} .

In table 2, we summarize the HNL production modes and decay channels for each effective operator of interest. We discuss the latter in the next subsection.

2.2 HNL decays

Pair- N_R operators. The pair- N_R interactions cannot make the HNL decay. Hence, in these scenarios, the N decay can proceed only via active-sterile-neutrino mixing. In this case, we use the formulae for the HNL decay width provided in Ref. [67].

Single- N_R operators. These operators lead to HNL decays even in the absence of active-sterile-neutrino mixing. We discuss the corresponding decay modes below.

- All single- N_R operators induce 5-body decays of N through an off-shell top quark, t^* , and an off-shell W -boson, W^* . For example, the decay chain triggered by \mathcal{O}_{duNe}^{33} is $N \rightarrow e^-t^*\bar{b} \rightarrow e^-bW^*\bar{b} \rightarrow e^-b\bar{b}(q'\bar{q} \text{ or } \ell^+\nu_\ell)$.⁵ Analogous decay chains for the other single- N_R operators are given in table 2.
- Operators containing two terms, one of which does not involve the top quark, trigger 3-body decays.⁶ There are five flavor structures in this category: \mathcal{O}_{LNQd}^{31} , \mathcal{O}_{LNQd}^{33} ,

⁵If m_N is large enough, this decay becomes either 4- or 3-body, with respectively an on-shell W or an on-shell t in the final state.

⁶We assume that m_N is sufficiently large for b -quark(s) to go on shell.

Operator		HNL production modes		HNL decay channels	
Name	Flavor	Top decay	pp collision	5-body	3-body
\mathcal{O}_{uN}	13	$t \rightarrow uN\bar{N}$	$pp \rightarrow tN\bar{N}$	\times	\times
\mathcal{O}_{QN}	13	$t \rightarrow uN\bar{N}$	$pp \rightarrow tN\bar{N}/bN\bar{N}$	\times	\times
\mathcal{O}_{QuNL}	13	$t \rightarrow u\bar{\nu}N/de^+N$	$pp \rightarrow t\nu\bar{N}/te^-\bar{N}$	$N \rightarrow \nu t^*\bar{u}/e^-t^*\bar{d}$	\times
	31	$t \rightarrow uv\bar{N}$	$pp \rightarrow t\bar{\nu}N/be^+N$	$N \rightarrow \nu u\bar{t}^*$	$N \rightarrow e^-u\bar{b}$
	33	$t \rightarrow be^+N$	\times	$N \rightarrow e^-t^*\bar{b}/\nu t^*\bar{t}^*$	\times
\mathcal{O}_{duNe}	13	$t \rightarrow de^+N$	$pp \rightarrow te^-\bar{N}$	$N \rightarrow e^-t^*\bar{d}$	\times
	33	$t \rightarrow be^+N$	\times	$N \rightarrow e^-t^*\bar{b}$	\times
\mathcal{O}_{LNQd}	31	$t \rightarrow de^+N$	$pp \rightarrow te^-\bar{N}/b\nu\bar{N}$	$N \rightarrow e^-t^*\bar{d}$	$N \rightarrow \nu b\bar{d}$
	33	$t \rightarrow be^+N$	\times	$N \rightarrow e^-t^*\bar{b}$	$N \rightarrow \nu b\bar{b}$

Table 2. HNL production models and tree-level decay channels induced by the four-fermion operators with N_R and third-generation quarks. Pair- N_R operators contribute only to HNL production, while single- N_R operators also induce 5-body and in some cases 3-body HNL decays. The virtual top quark t^* decays as $t^* \rightarrow bW^* \rightarrow b(q'\bar{q} \text{ or } \ell^+\nu)$. The operators \mathcal{O}_{LdQN}^{13} and \mathcal{O}_{LdQN}^{33} lead to the same processes as \mathcal{O}_{LNQd}^{31} and \mathcal{O}_{LNQd}^{33} , respectively.

\mathcal{O}_{LdQN}^{13} , \mathcal{O}_{LdQN}^{33} , and \mathcal{O}_{QuNL}^{31} , cf. table 1. For example, in the case of \mathcal{O}_{LNQd}^{33} , we have $N \rightarrow \nu b\bar{b}$. The corresponding 3-body decays for the other operator structures are shown in table 2.

- At the one-loop level, the operators leading to 5-body tree-level decays will also trigger 3-body decays. The corresponding decay rates can be sizable for the operators with a particular chiral structure. For example, the operators \mathcal{O}_{QuNL}^{13} and \mathcal{O}_{QuNL}^{33} contain light left-handed fields together with a right-handed top quark t_R , which can be easily turned to a left-handed top quark t_L by the large top Yukawa coupling and coupled to the W -boson [58]. The corresponding one-loop diagrams are shown in figure 4 for the case of \mathcal{O}_{QuNL}^{13} .

The relative contributions of these decay modes to the total HNL decay width will depend on the model parameters, *i.e.* the HNL mass, m_N , and the interaction couplings, c_O/Λ^2 and V_{eN} . To give an example, in what follows we consider three operator structures, \mathcal{O}_{duNe}^{33} , \mathcal{O}_{LNQd}^{33} , and \mathcal{O}_{QuNL}^{13} , and compare their contributions to the N decay width with that in the minimal scenario, characterized by active-sterile-neutrino mixing only.

In the upper-left panel of figure 5, we display the HNL partial decay widths induced

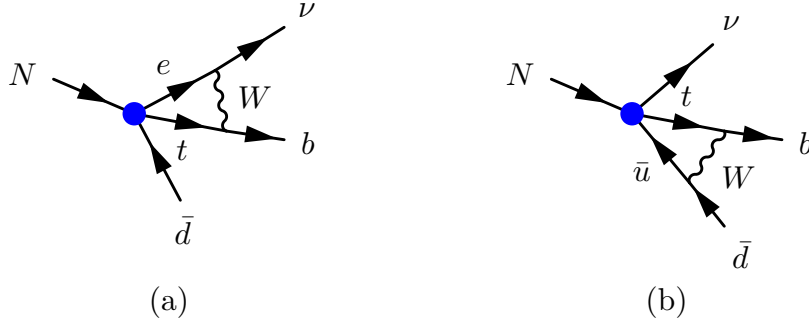


Figure 4. One-loop diagrams (in the unitary gauge) for the 3-body decay $N \rightarrow \nu b \bar{d}$ induced by the operator \mathcal{O}_{QuNL}^{13} .

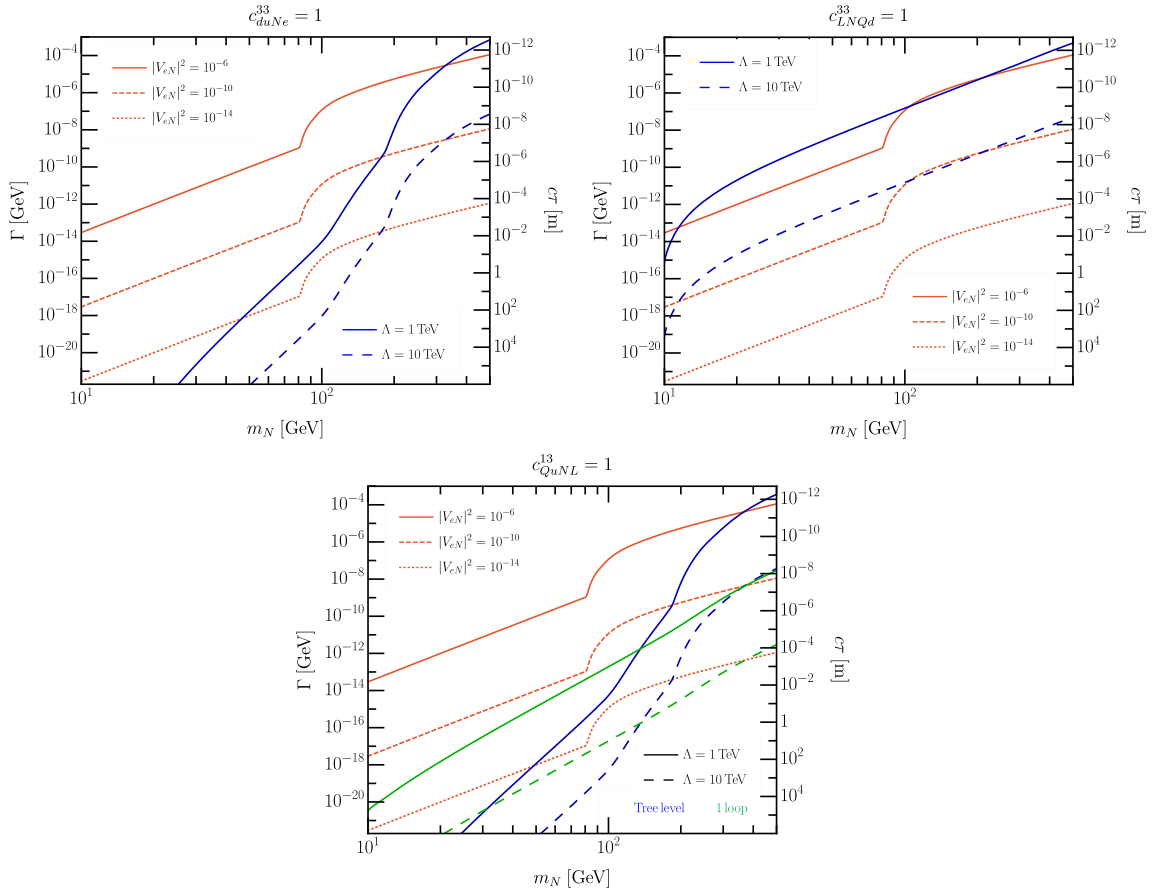


Figure 5. Mixing and operator contributions to the HNL decay width as a function of its mass. The operator contributions (blue and green lines) come from \mathcal{O}_{duNe}^{33} (top left), \mathcal{O}_{LNQd}^{33} (top right), and \mathcal{O}_{QuNL}^{13} (bottom), and we have set two values of Λ . Contributions from three values of $|V_{eN}|^2$ are shown for comparison in orange.

by \mathcal{O}_{duNe}^{33} , namely, $\Gamma(N \rightarrow e^- b \bar{b} q' \bar{q}) + \Gamma(N \rightarrow e^- b \bar{b} \ell^+ \nu_\ell)$, where $q' \bar{q} = \{u \bar{d}, u \bar{s}, c \bar{s}, c \bar{d}\}$ and

$\ell^+\nu_\ell = \{e^+\nu_e, \mu^+\nu_\mu, \tau^+\nu_\tau\}$.⁷ We have set $c_{duNe}^{33}/\Lambda^2 = 1/(1 \text{ TeV})^2$. For comparison, we show the mixing contribution to the decay width for three different values of the squared mixing parameter $|V_{eN}|^2$. Notice the y -axis spans around 20 orders of magnitude along the mass range under consideration. There are two sudden increases in the operator contribution, which occur at $m_N \simeq m_W + 2m_b$ and $m_N \simeq m_t + m_b$, as the decays to on-shell W -bosons and top quarks, respectively, become possible. A similar behavior can be observed in the mixing curves at $m_N \simeq m_W$, when the decay channel to on-shell W opens.

In the upper-right panel of figure 5, we show the HNL partial decay width of the 3-body decay $N \rightarrow \nu b \bar{b}$ triggered by the operator \mathcal{O}_{LNQd}^{33} (it dominates over the 5-body decays, which we do not show). We have set $c_{LNQd}^{33}/\Lambda^2 = 1/(1 \text{ TeV})^2$. The operator contribution wins over the mixing one if Λ is not too large, as $\Gamma_{\mathcal{O}} \propto \Lambda^{-4}$ and $\Gamma_{\text{mix}} \propto |V_{eN}|^2$.

In the bottom panel of figure 5, by the green lines we show the decay width of the 3-body decay $N \rightarrow \nu b \bar{d}$ induced by \mathcal{O}_{QuNL}^{13} through the one-loop diagrams depicted in figure 4. We have computed this decay width using the pipeline `FeynArts` [68] + `FormCalc` [69] + `LoopTools` [69]. We find perfect agreement with the corresponding result shown in figure 6 of Ref. [58]. The blue lines correspond to the sum of the “5-body” tree-level decay widths for $N \rightarrow e^- t^* \bar{d} \rightarrow e^- W^* b \bar{d} \rightarrow e^- b \bar{d} (q' \bar{q} \text{ or } \ell^+ \nu_\ell)$ and $N \rightarrow \nu_e t^* \bar{u} \rightarrow \nu_e W^* b \bar{u} \rightarrow \nu_e b \bar{u} (q' \bar{q} \text{ or } \ell^+ \nu_\ell)$, induced by \mathcal{O}_{QuNL}^{13} at tree-level and computed with `MadGraph5`. As can be seen, for $c_{QuNL}^{13}/\Lambda^2 = 1/(1 \text{ TeV})^2$, the loop-induced 3-body decay dominates over the tree-level 5-body decays for HNL masses up to approximately $m_N \approx 130 \text{ GeV}$.

In the case of \mathcal{O}_{QuNL}^{33} , we have a similar 3-body decay $N \rightarrow \nu b \bar{b}$. However, now, in addition to the diagrams with the W -boson in the loop, we also have diagrams with exchange of the Z -boson and the Higgs boson. We have checked that for $\Lambda = 1 \text{ TeV}$ and $m_N \gtrsim 15 \text{ GeV}$, this operator leads to prompt decays with $c\tau \lesssim 0.01 \text{ mm}$. Thus, we will not consider it in what follows among our benchmark scenarios featuring a long-lived HNL.

2.3 Benchmark scenarios

In section 4, we will study numerically a few representative scenarios, each characterized by an effective operator with given quark-flavor indices. We will switch on one operator structure at a time and investigate its phenomenological implications at the LHC main detector ATLAS, as well as at the current and future “far detector” facilities, including MoEDAL-MAPP2, MATHUSLA, ANUBIS and CODEX-b.

We describe the characteristic features of each selected scenario below, and we refer the reader to table 2 for a summary of the HNL production and decay modes.

1. \mathcal{O}_{uN}^{13} : Being a pair- N_R operator, it only contributes to pair production of HNLs. The dominant channel is $pp \rightarrow tN\bar{N}$, *cf.* the upper-left panel of figure 2. HNL decay, on the other hand, is completely controlled by the mixing parameter. We note in passing that a scenario with \mathcal{O}_{QN}^{13} would be qualitatively very similar.

⁷The decays to $q'\bar{q} = \{u\bar{b}, c\bar{b}\}$ are strongly suppressed by the corresponding small CKM elements. By summing over all possible final states we are taking into account the contributions from off-shell and on-shell top quark and W -boson.

2. \mathcal{O}_{QuNL}^{13} : This operator contributes to both HNL production and decay. As discussed above and shown in the bottom panel of figure 5, the 3-body decay induced at one loop dominates over 5-body decays induced at tree-level. In our numerical simulation, we will take into account both the 3-body decay via the operator and tree-level decays via mixing.
3. \mathcal{O}_{duNe}^{13} : This operator structure also contributes to both production and decay. HNLs are dominantly produced directly in pp collisions, as can be inferred from the upper-right panel of figure 2. The operator contribution to the decay is naturally suppressed (compared to mixing) for $m_N < m_W$, since the only allowed channel is a 5-body decay.⁸ This is no longer true for $m_N > m_W(m_t)$, when 4-body (3-body) decays are possible. Therefore, the operator contribution should be taken into account along with the mixing contribution.
4. \mathcal{O}_{duNe}^{33} : The operator contributes to HNL production and decay. However, production now occurs only through top quark decays, leading to smaller cross-sections than in the previous scenarios; see figure 2. As for the decay, analogously to scenarios 2 and 3, the operator contribution competes with the mixing one and has to be taken into account, *cf.* the upper-left panel of figure 5 and the related discussion.

3 Experiments and simulation

In this work, we consider not only the ATLAS experiment but also a series of proposed far detectors dedicated to LLP searches at the LHC.⁹ Here, we introduce these experiments and search strategies, and outline the simulation procedure employed for determining the sensitivity reach of these experiments to long-lived HNLs coupled to top quarks.

3.1 ATLAS

For the ATLAS experiment, we focus on a signature characterized by a DV arising from the HNL decay, accompanied by jets originating from either top quark decays or the HNL decay itself. The latest DV search with jets at ATLAS [70] is not optimal for our signal, mainly because of its too strong thresholds on the transverse momenta of jets and multi-jet cuts. Therefore, we propose a new search strategy with optimal jet cuts and the optional requirement of a b -jet. Our strategy is inspired by the recast [71] for the ATLAS “DV+jets” search [70] and by a past 8-TeV search for DVs at ATLAS [72].

We implement the operators of interest in a UFO file with `Feynrules` [73, 74]. With this model file, we then simulate HNL production in pp collisions at $\sqrt{s} = 14$ TeV using `MadGraph5` [64, 65] with the NNPDF3.1 PDF set [75]. For each benchmark scenario, we focus on the dominant production channel of the HNL: either direct pp collision in

⁸This is true only at tree-level. One can consider 3-body decays via W -loop.

Their contribution to the total decay width is negligible though for this particular operator structure.

⁹We do not simulate explicitly for the CMS experiment, for which we expect similar results.

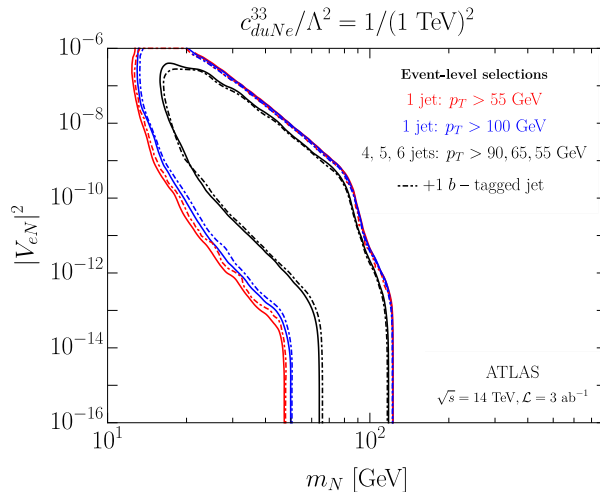


Figure 6. ATLAS sensitivity for one example operator, \mathcal{O}_{duNe}^{33} , in the plane $|V_{eN}|^2$ vs. m_N for the proposed complete search strategy with different jet-selection cuts at the event-level (see text for more details).

association with a top or bottom quark, or top quark decay if the former is absent (see table 2). We generate 100 thousand events at multiple parameter points in a grid covering the plane $|V_{eN}|^2$ vs. m_N , while keeping $c_{\mathcal{O}}^{ij}/\Lambda^2$ constant for each benchmark. HNL decays are then handled in `MadSpin` [76], where signal decays to final states with jets are enforced for numerical stability. In particular, we simulate the decay into ejj and νjj via mixing, and for benchmarks 2 – 4, we additionally simulate the HNL decays induced by the single- N_R operators, which all contain at least two jets.

The generated events are processed in `Pythia8` [77] for showering, hadronization, and event selections. Truth jets are reconstructed using `FastJet` [78], with the anti- k_t algorithm and $R = 0.4$, excluding neutrinos and muons. This jet definition includes particles from the HNL decays. Event selection proceeds in two stages: (1) event-level selections; and (2) DV-level selections.

Event-level selections: we impose preliminary selections based on the number of jets in the event meeting specific p_T -criteria — events must have 4, 5, or 6 jets with $p_T > 90, 65$, or 55 GeV, respectively, following Ref. [72]. This choice of multi-jet cuts enhances the sensitivity to our signal, as opposed to considering the jet selections imposed in the recast done in Ref. [71]. The search [70] that was recast in that paper was intended for directly pair-produced LLPs (decaying to several jets). For our benchmarks, sensitivity is largely lost at the event-level when using these 13-TeV-search jet cuts [70], and therefore we propose to retain the jet- p_T thresholds as low as the ATLAS 8-TeV search [72].¹⁰

¹⁰This proposal can be further justified by the potential and prospective leverage that some specialized data taking techniques (*i.e.* such as data parking [79]) can have on beyond the Standard Model physics on data collected with low triggering thresholds. Such techniques were used by LHC experiments in searches for HNLs; see *e.g.* Ref. [80].

In figure 6, we show the impact on the sensitivity limits to one of our benchmarks when requiring different jet- p_T thresholds. When aiming at discovery prospects, one may further consider identifying b -quark jets associated to our event signatures (see table 2). We treat a jet as a b -jet based on the flavor of the truth quark that initiated the jet. From all truth jets in the event with $p_T > 20$ GeV and $|\eta| < 2.5$, we tag a jet as a b -jet if a Monte-Carlo truth b -quark with $p_T > 5$ GeV is found within a cone of size $\Delta R = 0.3$ around the jet direction. We additionally force a flat b -jet identification efficiency of 77% [81].

DV-level selections: we implement DV reconstruction according to the recast [71] of the ATLAS “DV+jets” search [70], where at least one vertex in the event must satisfy the following conditions:

1. The transverse distance from the vertex to the IP must be within $4 \text{ mm} < R_{xy} < 300 \text{ mm}$ and the longitudinal position of the vertex must satisfy $|z| < 300 \text{ mm}$.
2. At least one track should have an absolute transverse impact parameter $|d_0| > 2 \text{ mm}$.
3. The DV must contain at least 5 tracks all satisfying the two requirements below:
 - (a) They should have a boosted transverse decay length larger than 520 mm.
 - (b) Their p_T and charge q should satisfy $p_T/|q| > 1 \text{ GeV}$.
4. The invariant mass of the DV, reconstructed from the tracks passing the above requirements for which the masses are all assumed to be that of a charged pion, should be larger than 10 GeV.

The ATLAS collaboration [70] provided parameterized efficiencies at both event level and vertex level, to account for further, more intricate event selections that are difficult to simulate, for recasting purpose. The event-level (vertex-level) efficiencies¹¹ are functions of the transverse position of the DV and the sum of the truth-jet p_T (the transverse position of the DV, the number of charged particles associated to the truth decay vertex, as well as the vertex invariant mass). We apply the parameterized efficiencies at vertex-level only, in our proposed search. Thus, the events that pass the jet-selection criteria and contain at least one reconstructed vertex meeting the above requirements contribute to the final signal-efficiency cutflow.

The expected number of signal events at ATLAS is calculated with

$$\begin{aligned}
N_S^{\text{ATLAS}} &= \sigma \cdot \mathcal{L} \cdot \left\{ \mathcal{B}_{\text{mix}} \cdot \varepsilon^{\text{mix}} + \mathcal{B}_{\text{op}} \cdot \varepsilon^{\text{op}} \right\}, \\
\mathcal{B}_{\text{mix}} &= \mathcal{B}(N \rightarrow ejj) + \mathcal{B}(N \rightarrow \nu jj), \\
\mathcal{B}_{\text{op}} &= \mathcal{B}(N \rightarrow 5\text{-body tree}) + \mathcal{B}(N \rightarrow 3\text{-body loop}),
\end{aligned} \tag{3.1}$$

where σ is the production cross-section of the HNL N , $\mathcal{L} = 3 \text{ ab}^{-1}$ is the integrated luminosity, and $\mathcal{B}_{\text{mix/op}}$ represents the sum of the branching fractions of the HNL decay modes

¹¹The ATLAS search [70] employs two signal regions, the strong one and the electroweak one. The two SRs share the same vertex-level efficiencies.

of interest induced by the mixing or the operator. We remark that the latter term is not present in benchmark 1. Here, “ j ” denotes a jet including the up, down, charm, strange, or bottom quark. The final cutflow efficiencies, $\varepsilon^{\text{mix/op}}$, are the ones obtained from implementing both event- and vertex-level selections in each case (including the acceptances and parameterized efficiencies) to the final states induced via mixing/operator in our custom code implemented within `Pythia8`.

We note that the vertex-level selection criteria are designed to suppress all backgrounds,¹² allowing us to derive the 95% C.L. exclusion limits by requiring at least 3 signal events. We additionally provide exclusion limits for 10 and 30 signal events for certain scenarios, which would correspond to the exclusion limits at the same level if approximately 25 and 225 background events were present, respectively.

3.2 Far detectors

Several proposals of a far detector displaced relative to different interaction points (IPs) at the LHC have been brought up in the last decade, such as FASER(2) [82, 83], CODEX-b [84, 85], MATHUSLA [1, 59, 86], ANUBIS [60], FACET [87], and MoEDAL-MAPP1(2) [88, 89]. They are supposed to be detector systems with tracking capabilities enabling reconstruction of displaced vertices consisting of charged particles, to be placed about 5–500 meters from various IPs. The LLPs, once produced *e.g.* at an IP, can travel towards a far detector and decay inside. The macroscopic distances between these experiments and the IPs allow for implementation of efficient veto and shielding of potential background events, leading to expected vanishing background level at these experiments in general, even with an integrated luminosity as large as 3 ab^{-1} . We note that FASER has been approved and its operation has been launched.

These experiments can be classified into two categories according to their relative direction with respect to their corresponding IPs, namely, transverse detectors (MATHUSLA, ANUBIS, MoEDAL-MAPP1(2), and CODEX-b) and forward detectors (FASER(2) and FACET). In the present work, the long-lived HNLs are assumed to stem from either top quark decays or direct production in pp collisions. The HNLs thus produced tend to travel in the transverse direction. Therefore, we will not discuss further the forward experiments which we have numerically checked and verified to have no sensitivities. Among the transverse detectors, MATHUSLA and ANUBIS would be constructed in the vicinity of the CMS and ATLAS IPs, respectively, both with a projected integrated luminosity of 3 ab^{-1} in the HL-LHC era. The MATHUSLA experiment would be a box-shaped detector to be instrumented on the ground surface, with a 68 m (60 m) distance in the horizontal (vertical) direction from the IP. It would have a designed geometrical size of $100 \text{ m} \times 100 \text{ m} \times$

¹²The ATLAS DV+jets search in Ref. [70] applies stricter cuts on jet- p_T thresholds. However, in that search, background suppression is driven primarily by DV requirements rather than by requirements on the jets in the event, justifying our assumption that the DV selections alone are sufficient to eliminate the background events.

25 m.¹³ ANUBIS has been proposed to be installed inside a service shaft above the ATLAS IP, with about 5 m horizontal distance in the beam direction from the IP. It has cylindrical shape with a diameter of 18 m and a height of 54 m.¹⁴ MoEDAL-MAPP1(2) and CODEX-b are both proposed far detectors related to the LHCb IP8. CODEX-b would be cubic with dimensions 10 m \times 10 m \times 10 m, placed 25 m from the IP. The pseudorapidity η and azimuthal-angle ϕ coverages are respectively $\eta \in [0.2, 0.6]$ and $\frac{\delta\phi}{2\pi} \sim \frac{0.4}{2\pi}$. It is projected to receive data of 300 fb⁻¹ at the end of the HL-LHC phase. MoEDAL-MAPP1 and MAPP2 are proposed as trapezoidal-shaped detectors to be implemented in the UGCI gallery. The MAPP1 detector would have a volume of 130 m³ and the MAPP2 is an extended version of MAPP1, with a volume of 430 m³. MAPP1 has a polar angle of 5° and a distance of 55 m, relative to the IP, and MAPP2 would take up the space of the whole gallery. For these two experiments, the expected integrated luminosities are 30 fb⁻¹ and 300 fb⁻¹, as they should be operated during the LHC Run3 and the HL-LHC periods, respectively.

For computing the sensitivity of the far detectors, we follow a somewhat different procedure than that used for ATLAS, as we do not simulate the HNL decay in this case. We start by generating 100 thousand events for various HNL masses using `MadGraph5` and pass the resulting Les Houches Event Files (LHEF) [92] directly to `Pythia8`. We then calculate the probability for the HNL to decay within each far detector, and derive the average decay probability over all the simulated HNLs,

$$\langle P [N \text{ decay in f.v.}] \rangle = \frac{1}{k} \sum_{i=1}^k P [N^i \text{ decay in f.v.}], \quad (3.2)$$

where $k = 10^5$ or 2×10^5 , depending on whether in each signal event one or two HNLs are produced, is the total number of the simulated HNLs for each HNL mass, “f.v.” stands for fiducial volume, and the probability in each case is determined by the HNL’s boosted decay length and momentum angle besides the geometry and position of the far detectors. The expected number of signal events at the far detectors is then given by:

$$N_S^{\text{FD}} = \sigma \cdot \mathcal{L} \cdot \langle P [N \text{ decay in f.v.}] \rangle \cdot \mathcal{B}(N \rightarrow \text{vis.}) \cdot \varepsilon, \quad (3.3)$$

where σ and $\mathcal{L} = 3 \text{ ab}^{-1}$ are respectively the production cross-section and the integrated luminosity of the HL-LHC era. $\mathcal{B}(N \rightarrow \text{vis.})$ denotes the decay branching ratio of the HNL into visible final states (that can be induced either via mixing or the operator), for which we have only excluded the fully invisible tri-neutrino final states. We assume a detection efficiency of $\varepsilon = 100\%$ for simplicity.

As vanishing background is expected at the far detectors, we derive the 95% C.L. exclusion limits by requiring 3 signal events. However, MATHUSLA and ANUBIS might

¹³Recently a smaller version has been suggested for cost-related reasons [90]. However, since it is still in the developing stage, we stick to the latest design [86].

¹⁴In Ref. [91] a new geometrical design of ANUBIS has been proposed, where the apparatus is supposed to be instrumented on the ATLAS cavern ceiling or at the bottom of a shaft. As the design has not been finalized, we choose to focus on the original proposal.

change the detector geometries (and thus the total acceptance) from the original designs, and ANUBIS with its relatively close distance from the IP might suffer from a non-zero level of background events. Therefore, we will also provide sensitivity limits for larger numbers of signal events using the original designs, to facilitate deriving sensitivities corresponding to other values of the acceptances or background levels.

4 Numerical results

In this section, we present the numerical results obtained using the simulation procedure outlined above. We analyze the sensitivities of ATLAS and the far detectors, focusing on the four benchmark scenarios defined in section 2.3, characterized by different effective operators containing a top quark and at least one HNL. In each case, a single effective operator structure is switched on, together with the standard active-sterile-neutrino mixing. The mixing parameter $|V_{\ell N}|^2$, the HNL mass m_N , and the operator coefficients $c_{\mathcal{O}}^{ij}/\Lambda^2$ are treated as independent parameters. For simplicity, we consider a single kinematically relevant HNL that mixes exclusively with electron neutrinos, *i.e.* $V_{\ell N} = V_{eN}$.

We note that for the plots of the results shown in this section, we do not assume that the bottom quarks in the event have been tagged. Thus, our regions are, strictly speaking, not discovery regions but exclusion prospects. We choose to do so, to obtain a fair comparison of the far detectors and ATLAS, because only ATLAS can identify the top quark(s) in the event. However, as shown in figure 6, discovery regions (including b -tagging) are similar to, albeit slightly smaller than, exclusion prospects in the ATLAS simulation.

The benchmark scenarios are divided into two categories: pair- N_R operators (scenario 1) and single- N_R operators (scenarios 2–4). For pair- N_R operators, HNL production is dominated by the operator, while the HNL decays occur solely via mixing, resulting in decoupled production and decay processes. In this case, the mixing parameter V_{eN} drives leptonic and semileptonic HNL decays through off-shell or on-shell W - and Z -bosons, depending on the HNL mass. Conversely, for single- N_R operators, the operator contributes to both production and decay, with the latter potentially dominating over the mixing in some parts of the parameter space. In either case, the final states containing charged particles are detectable by the far detectors, while the final states with jets contribute to the searched signal in ATLAS.

In figure 7, we display the sensitivity contours of ATLAS and the far detectors in the $|V_{eN}|^2$ vs. m_N plane. The upper-left panel corresponds to scenario 1, where the pair- N_R operator structure \mathcal{O}_{uN}^{13} is switched on, assuming $c_{uN}^{13} = 1$ and $\Lambda = 1$ TeV. Solid lines correspond to 3 signal events, while dashed lines, which are present for MATHUSLA, ANUBIS, and ATLAS, are for 30 signal events.¹⁵ Since the production process is controlled by the op-

¹⁵Note that the smaller version of MATHUSLA, recently discussed in Ref. [90] is roughly a factor 10 smaller in volume than the original MATHUSLA design [86], used in our simulation. The 30-event lines thus correspond roughly to the 3-event curves of the smaller design.

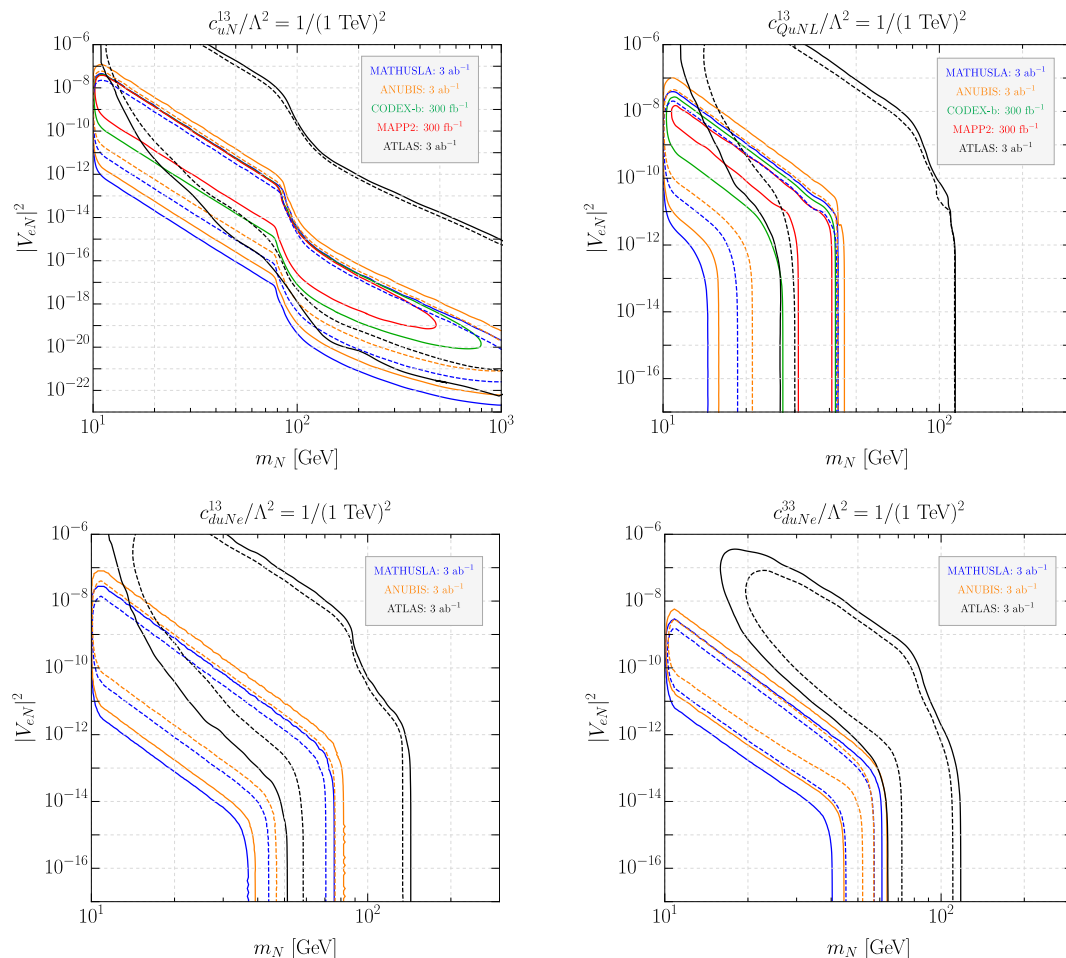


Figure 7. Sensitivities of ATLAS and the far detectors in the plane $|V_{eN}|^2$ vs. m_N to scenarios 1 (top left), 2 (top right), 3 (bottom left), and 4 (bottom right). Solid lines correspond to 3 signal events. Dashed lines are for 30 events in all the plots, except for the lower-right panel, where they correspond to 10 events.

erator coefficient and decoupled from decay, these experiments can probe very small values of active-sterile-neutrino mixing and large HNL masses. Among the far detectors, MATHUSLA and ANUBIS exhibit the strongest sensitivities, reaching HNL masses in excess of 1 TeV. However, the EFT validity requires m_N to be significantly below the new-physics scale, and we limit the plot range accordingly for our choice of $\Lambda = 1$ TeV. CODEX-b and MAPP2 cover smaller regions of the parameter space, but still can reach values of $|V_{eN}|^2$ as low as 10^{-20} and 10^{-19} , respectively, and masses up to 800 GeV (CODEX-b) and 500 GeV (MAPP2). Compared to the far detectors, ATLAS can probe larger values of mixing for the same HNL mass range, because of its better sensitivity to LLPs with shorter lifetimes. The nearly 4π angular coverage further enhances its capabilities.

The sensitivities to single- N_R operator scenarios are shown in the other panels of figure 7. In the upper-right panel, we switch on the operator \mathcal{O}_{QuNL}^{13} (scenario 2), and

in the lower-left and lower-right panels, we consider the operators \mathcal{O}_{duNe}^{13} (scenario 3) and \mathcal{O}_{duNe}^{33} (scenario 4), respectively. For these plots, we assume the respective operator coefficient $c_{\mathcal{O}}^{ij} = 1$ and $\Lambda = 1$ TeV. The solid and dashed lines follow the same conventions as in scenario 1, except for the lower-right panel, where dashed lines correspond to 10 signal events as a result of the smaller HNL production cross-section in scenario 4 (see figure 2).

In all the three single- N_R operator scenarios, the sensitivity curves exhibit a funnel-like feature in a certain mass region, *i.e.* a region where the sensitivity curves become independent of the mixing parameter. More specifically, in this mass region, the chosen value of the operator coefficient alone leads to more than 3 (30) signal events inside the solid (dashed) contour. In general, this funnel-like behavior appears when the operator starts to dominate the HNL decay, generating sufficient number of signal events even when the mixing parameter is negligible. Note, however, this does not imply sensitivity to infinitely small values of mixing: if the operator did not contribute to the HNL decay, the sensitivity regions in the $|V_{eN}|^2$ vs. m_N plane would be bounded from below. The upper mass reach in these scenarios is limited by the size of the detectors — for larger masses, the HNLs decay too promptly to leave an imprint in the far detectors or produce a displaced vertex in ATLAS.

There are qualitative differences among these scenarios. In scenario 2 with the \mathcal{O}_{QuNL} operator (upper-right panel), the sensitivity in mass is limited to $m_N \lesssim 40$ GeV for the far detectors because of the larger decay width with this operator in this mass range. In contrast, for scenarios 3 and 4 (bottom panels), the far detectors can probe larger masses, with sensitivities up to $m_N \lesssim 80$ GeV. On the other hand, ATLAS is sensitive to $m_N \lesssim 120$ GeV in all three scenarios. Moreover, only the experiments with an expected integrated luminosity of $\mathcal{L} = 3$ ab $^{-1}$ (MATHUSLA, ANUBIS, and ATLAS) exhibit sensitivity to scenarios 3 and 4. This is because the operator \mathcal{O}_{duNe} generates smaller production cross-sections compared to \mathcal{O}_{uN} and \mathcal{O}_{QuNL} , requiring higher luminosities for detection.

We also explore the sensitivity limits in the Λ vs. m_N plane for fixed values of the active-sterile-neutrino mixing. They are displayed in the four panels of figure 8, corresponding to the operators \mathcal{O}_{uN}^{13} (top left), \mathcal{O}_{QuNL}^{13} (top right), \mathcal{O}_{duNe}^{13} (bottom left), and \mathcal{O}_{duNe}^{33} (bottom right). We show the reach in Λ for two mixing values: $|V_{eN}|^2 = 10^{-10}$ (solid lines)¹⁶ and $|V_{eN}|^2 = 10^{-18}$ (dashed lines). The chosen values of the mixing parameter allow us to neglect either the operator or the mixing contribution to the HNL decay, such that we have a simple scaling of the number of signal events with Λ . In all four scenarios considered, we observe that (i) the probed HNL masses depend strongly on the assumed value of $|V_{eN}|^2$, and (ii) for the same value of $|V_{eN}|^2$, ATLAS and the far detectors cover complementary mass ranges. The accessible parameter space varies significantly between scenarios. Scenario 1 exhibits the highest sensitivities in both m_N and Λ . In particular, for $|V_{eN}|^2 = 10^{-10}$, ATLAS can probe the new-physics scale Λ in excess of 10 TeV for 40 GeV $\lesssim m_N \lesssim 80$ GeV. MATHUSLA (ANUBIS) reaches $\Lambda \approx 4.5$ (4) TeV for m_N

¹⁶For scenario 2, we have fixed instead $|V_{eN}|^2 = 10^{-9}$ to guarantee that the operator contribution to the HNL decay is negligible compared to the mixing one; see the bottom panel in figure 5.

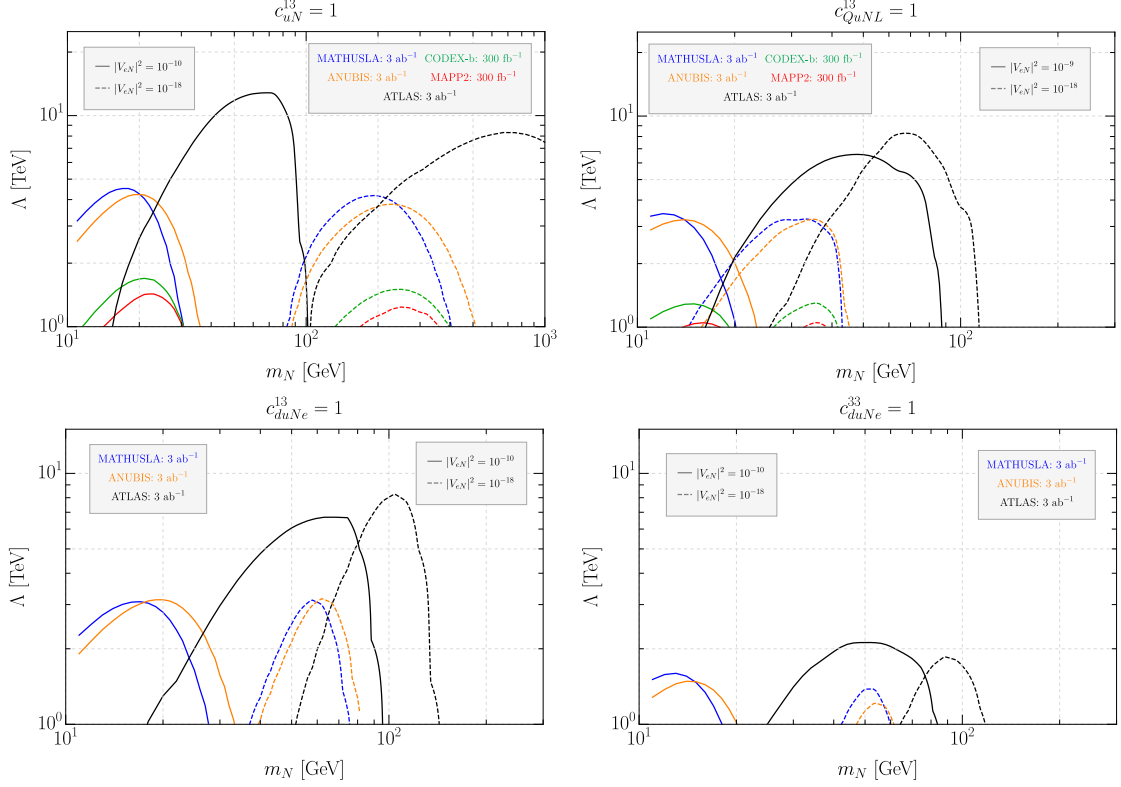


Figure 8. Sensitivities of ATLAS and the far detectors in the plane Λ vs. m_N to scenarios 1 (top left), 2 (top right), 3 (bottom left), and 4 (bottom right). Solid (dashed) lines correspond to $|V_{eN}|^2 = 10^{-10}$ (10^{-18}), except for scenario 2, where solid lines are for $|V_{eN}|^2 = 10^{-9}$.

slightly smaller than 20 GeV, whereas CODEX-b (MAPP2) can exclude $\Lambda \lesssim 1.5$ (1.2) TeV for m_N slightly larger than 20 GeV. Assuming $|V_{eN}|^2 = 10^{-18}$, a similar reach in Λ occurs for $m_N \gtrsim 100$ GeV. In scenario 2, ATLAS can reach $\Lambda \approx 7$ TeV (more than 8 TeV) for m_N around 50 (70) GeV if $|V_{eN}|^2 = 10^{-9}$ (10^{-18}). MATHUSLA and ANUBIS can be sensitive to the scales as large as 3 TeV, whereas the sensitivities of CODEX-b and MAPP2 extend to only slightly above $\Lambda = 1$ TeV. Scenario 3 exhibits similar sensitivities, with ATLAS being capable of probing Λ values up to 7–8 TeV, and MATHUSLA and ANUBIS being sensitive to new-physics scales of up to 3 TeV. However, the far detectors in this scenario can probe larger masses than those in scenario 2, for the same values of $|V_{eN}|^2$. In contrast, for scenario 4, the sensitivities are generally much weaker. Its limited reach is a result of the small production cross-sections, which result in insufficient numbers of HNLs even for moderate values of Λ . In fact, CODEX-b and MAPP2 are not sensitive at all to scenarios 3 and 4 for the same reason, while ATLAS can only probe $\Lambda \approx 2$ TeV in a relatively small m_N range in the latter scenario.

5 Conclusions

In the framework of N_R SMEFT, we have considered a set of the four-fermion operators with top quarks and HNLs; see table 1. Such operators may originate at low energies as a result of new heavy top-philic physics. We have studied HNL production and decay channels triggered by these effective interactions at the HL-LHC. The resulting phenomenology depends strongly on (i) the HNL mass, m_N , (ii) the type and strength of the effective interaction encoded in the ratio $c_{\mathcal{O}}^{ij}/\Lambda^2$ of the Wilson coefficient and the new-physics scale Λ , as well as (iii) the value of active-sterile-neutrino mixing V_{eN} .

In the present study, we have focused on long-lived, massive HNLs, that can leave a DV signature either in a local LHC detector, *e.g.* ATLAS or CMS, or in a planned far detector, *e.g.* MATHUSLA or ANUBIS. Depending on the type and the quark-flavor structure of the effective operator, HNLs can be produced at the LHC either directly in pp collisions or in rare top quark decays, *cf.* figures 1 and 3, and table 2. In the case of pair- N_R operators, HNL production and decay are decoupled, since the latter can only occur via active-sterile-neutrino mixing. For simplicity, we have assumed only one kinematically accessible HNL. On the other hand, single- N_R operators contribute to both HNL production and decay. We have computed the corresponding production cross-sections and decay rates; see figures 2 and 5, showing, in particular, how the latter compare to the decay rates induced by the active-sterile-neutrino mixing parameter V_{eN} .

We have further identified four benchmark scenarios possessing different phenomenology, each corresponding to a certain operator structure: \mathcal{O}_{uN}^{13} in the pair- N_R category, and \mathcal{O}_{QuNL}^{13} , \mathcal{O}_{duNe}^{13} , and \mathcal{O}_{duNe}^{33} in the single- N_R category. We have studied in detail the prospects for probing each of these four scenarios at the HL-LHC. For the ATLAS main detector we have proposed a search strategy based on published ATLAS searches for LLPs, and for the LHC far detectors we simply count the visible-decay numbers of the HNLs inside their fiducial volumes. Performing state-of-the-art numerical simulations, we have shown that in the case of \mathcal{O}_{uN}^{13} , assuming $c_{uN}^{13}/\Lambda^2 = 1 \text{ TeV}^{-2}$, MATHUSLA (ANUBIS) can probe $|V_{eN}|^2 \approx 10^{-20}$ (and even smaller) for $m_N \gtrsim 120$ (150) GeV,¹⁷ whereas ATLAS will be sensitive to such tiny values of the mixing for larger HNL masses, *cf.* figure 7. For a fixed value of $|V_{eN}|^2 = 10^{-10}$, MATHUSLA (ANUBIS) will be able to exclude the new-physics scale $\Lambda \lesssim 4.5$ (4) TeV for $m_N \approx 20$ GeV, whereas ATLAS will be sensitive to the scales in excess of 10 TeV for $40 \text{ GeV} \lesssim m_N \lesssim 80 \text{ GeV}$, as can be inferred from figure 8. A weaker reach in $|V_{eN}|^2$ and Λ is observed for the single- N_R scenarios. The key difference with respect to a pair- N_R interaction is that at a certain value of m_N , a single- N_R operator starts to dominate the HNL decay (with respect to the contributions from the active-sterile-neutrino mixing) resulting in the funnel-like feature on the corresponding plots in figure 7. The reach in Λ depends significantly on the operator structure.

¹⁷Here we quote the numbers obtained under the assumption of zero background. In figure 7, we have also provided the contours corresponding to a larger number of signal events to give an idea for more realistic experimental conditions.

For example, in the case of \mathcal{O}_{duNe}^{13} (\mathcal{O}_{duNe}^{33}), ATLAS can probe the new-physics scale as large as 7 (2) TeV for m_N around 50–60 GeV.

In conclusion, the proposed DV searches at ATLAS and future far detectors at the HL-LHC, including MATHUSLA and ANUBIS, provide a very sensitive tool for probing so far unconstrained HNL-related top-philic new physics that may be hiding at a few TeV scale.

Acknowledgements

We thank Juan Carlos Helo for useful discussions. This work is supported by the Spanish grants PID2023-147306NB-I00 and CEX2023-001292-S (MCIU/AEI/10.13039/501100011033), as well as CIPROM/2021/054 (Generalitat Valenciana). R.B. acknowledges financial support from the Generalitat Valenciana (grant ACIF/2021/052). G.C. acknowledges support from ANID FONDECYT grant No. 11220237 and ANID – Millennium Science Initiative Program ICN2019_044.

References

- [1] D. Curtin et al., *Long-Lived Particles at the Energy Frontier: The MATHUSLA Physics Case*, *Rept. Prog. Phys.* **82** (2019) 116201 [[1806.07396](#)].
- [2] L. Lee, C. Ohm, A. Soffer and T.-T. Yu, *Collider Searches for Long-Lived Particles Beyond the Standard Model*, *Prog. Part. Nucl. Phys.* **106** (2019) 210 [[1810.12602](#)].
- [3] J. Alimena et al., *Searching for long-lived particles beyond the Standard Model at the Large Hadron Collider*, *J. Phys. G* **47** (2020) 090501 [[1903.04497](#)].
- [4] J.L. Feng et al., *The Forward Physics Facility at the High-Luminosity LHC*, *J. Phys. G* **50** (2023) 030501 [[2203.05090](#)].
- [5] P.D. Bolton, F.F. Deppisch and P.S. Bhupal Dev, *Neutrinoless double beta decay versus other probes of heavy sterile neutrinos*, *JHEP* **03** (2020) 170 [[1912.03058](#)].
- [6] P.D. Bolton, F.F. Deppisch and P.S.B. Dev, *Probes of Heavy Sterile Neutrinos*, in *56th Rencontres de Moriond on Electroweak Interactions and Unified Theories*, 6, 2022 [[2206.01140](#)].
- [7] G. Cottin, J.C. Helo and M. Hirsch, *Searches for light sterile neutrinos with multitrack displaced vertices*, *Phys. Rev. D* **97** (2018) 055025 [[1801.02734](#)].
- [8] G. Cottin, J.C. Helo and M. Hirsch, *Displaced vertices as probes of sterile neutrino mixing at the LHC*, *Phys. Rev. D* **98** (2018) 035012 [[1806.05191](#)].
- [9] M. Drewes and J. Hajer, *Heavy Neutrinos in displaced vertex searches at the LHC and HL-LHC*, *JHEP* **02** (2020) 070 [[1903.06100](#)].
- [10] K. Bondarenko, A. Boyarsky, M. Ovchinnikov, O. Ruchayskiy and L. Shchutska, *Probing new physics with displaced vertices: muon tracker at CMS*, *Phys. Rev. D* **100** (2019) 075015 [[1903.11918](#)].

- [11] J. Liu, Z. Liu, L.-T. Wang and X.-P. Wang, *Seeking for sterile neutrinos with displaced leptons at the LHC*, *JHEP* **07** (2019) 159 [[1904.01020](#)].
- [12] F. Deppisch, S. Kulkarni and W. Liu, *Heavy neutrino production via Z' at the lifetime frontier*, *Phys. Rev. D* **100** (2019) 035005 [[1905.11889](#)].
- [13] C.-W. Chiang, G. Cottin, A. Das and S. Mandal, *Displaced heavy neutrinos from Z' decays at the LHC*, *JHEP* **12** (2019) 070 [[1908.09838](#)].
- [14] F.F. Deppisch, W. Liu and M. Mitra, *Long-lived Heavy Neutrinos from Higgs Decays*, *JHEP* **08** (2018) 181 [[1804.04075](#)].
- [15] S. Amrith, J.M. Butterworth, F.F. Deppisch, W. Liu, A. Varma and D. Yallup, *LHC Constraints on a $B - L$ Gauge Model using Contur*, *JHEP* **05** (2019) 154 [[1811.11452](#)].
- [16] I. Doršner, S. Fajfer, A. Greljo, J.F. Kamenik and N. Košnik, *Physics of leptoquarks in precision experiments and at particle colliders*, *Phys. Rept.* **641** (2016) 1 [[1603.04993](#)].
- [17] G. Cottin, O. Fischer, S. Mandal, M. Mitra and R. Padhan, *Displaced neutrino jets at the LHeC*, *JHEP* **06** (2022) 168 [[2104.13578](#)].
- [18] F. del Aguila, S. Bar-Shalom, A. Soni and J. Wudka, *Heavy Majorana Neutrinos in the Effective Lagrangian Description: Application to Hadron Colliders*, *Phys. Lett. B* **670** (2009) 399 [[0806.0876](#)].
- [19] A. Aparici, K. Kim, A. Santamaria and J. Wudka, *Right-handed neutrino magnetic moments*, *Phys. Rev. D* **80** (2009) 013010 [[0904.3244](#)].
- [20] Y. Liao and X.-D. Ma, *Operators up to Dimension Seven in Standard Model Effective Field Theory Extended with Sterile Neutrinos*, *Phys. Rev. D* **96** (2017) 015012 [[1612.04527](#)].
- [21] N.F. Bell, V. Cirigliano, M.J. Ramsey-Musolf, P. Vogel and M.B. Wise, *How magnetic is the Dirac neutrino?*, *Phys. Rev. Lett.* **95** (2005) 151802 [[hep-ph/0504134](#)].
- [22] M.L. Graesser, *Broadening the Higgs boson with right-handed neutrinos and a higher dimension operator at the electroweak scale*, *Phys. Rev. D* **76** (2007) 075006 [[0704.0438](#)].
- [23] M.L. Graesser, *Experimental Constraints on Higgs Boson Decays to TeV-scale Right-Handed Neutrinos*, **0705.2190**.
- [24] H.-L. Li, Z. Ren, M.-L. Xiao, J.-H. Yu and Y.-H. Zheng, *Operator bases in effective field theories with sterile neutrinos: $d \leq 9$* , *JHEP* **11** (2021) 003 [[2105.09329](#)].
- [25] R. Beltrán, R. Cepedello and M. Hirsch, *Tree-level UV completions for N_R SMEFT $d = 6$ and $d = 7$ operators*, *JHEP* **08** (2023) 166 [[2306.12578](#)].
- [26] I. Bischer and W. Rodejohann, *General neutrino interactions from an effective field theory perspective*, *Nucl. Phys. B* **947** (2019) 114746 [[1905.08699](#)].
- [27] M. Chala and A. Titov, *One-loop matching in the SMEFT extended with a sterile neutrino*, *JHEP* **05** (2020) 139 [[2001.07732](#)].
- [28] T. Li, X.-D. Ma and M.A. Schmidt, *General neutrino interactions with sterile neutrinos in light of coherent neutrino-nucleus scattering and meson invisible decays*, *JHEP* **07** (2020) 152 [[2005.01543](#)].
- [29] T. Li, X.-D. Ma and M.A. Schmidt, *Constraints on the charged currents in general neutrino interactions with sterile neutrinos*, *JHEP* **10** (2020) 115 [[2007.15408](#)].

- [30] G. Zhou, J.Y. Günther, Z.S. Wang, J. de Vries and H.K. Dreiner, *Long-lived sterile neutrinos at Belle II in effective field theory*, *JHEP* **04** (2022) 057 [[2111.04403](#)].
- [31] A. Caputo, P. Hernandez, J. Lopez-Pavon and J. Salvado, *The seesaw portal in testable models of neutrino masses*, *JHEP* **06** (2017) 112 [[1704.08721](#)].
- [32] J. Jones-Pérez, J. Masias and J.D. Ruiz-Álvarez, *Search for Long-Lived Heavy Neutrinos at the LHC with a VBF Trigger*, *Eur. Phys. J. C* **80** (2020) 642 [[1912.08206](#)].
- [33] D. Barducci, E. Bertuzzo, A. Caputo, P. Hernandez and B. Mele, *The see-saw portal at future Higgs Factories*, *JHEP* **03** (2021) 117 [[2011.04725](#)].
- [34] F. Delgado, L. Duarte, J. Jones-Perez, C. Manrique-Chavil and S. Peña, *Assessment of the dimension-5 seesaw portal and impact of exotic Higgs decays on non-pointing photon searches*, *JHEP* **09** (2022) 079 [[2205.13550](#)].
- [35] L. Duarte, J. Jones-Pérez and C. Manrique-Chavil, *Bounding the Dimension-5 Seesaw Portal with non-pointing photon searches*, *JHEP* **04** (2024) 133 [[2311.17989](#)].
- [36] J.M. Butterworth, M. Chala, C. Englert, M. Spannowsky and A. Titov, *Higgs phenomenology as a probe of sterile neutrinos*, *Phys. Rev. D* **100** (2019) 115019 [[1909.04665](#)].
- [37] J. De Vries, H.K. Dreiner, J.Y. Günther, Z.S. Wang and G. Zhou, *Long-lived Sterile Neutrinos at the LHC in Effective Field Theory*, *JHEP* **03** (2021) 148 [[2010.07305](#)].
- [38] R. Beltrán, G. Cottin, J.C. Helo, M. Hirsch, A. Titov and Z.S. Wang, *Long-lived heavy neutral leptons from mesons in effective field theory*, *JHEP* **01** (2023) 015 [[2210.02461](#)].
- [39] G. Cottin, J.C. Helo, M. Hirsch, A. Titov and Z.S. Wang, *Heavy neutral leptons in effective field theory and the high-luminosity LHC*, *JHEP* **09** (2021) 039 [[2105.13851](#)].
- [40] R. Beltrán, G. Cottin, J.C. Helo, M. Hirsch, A. Titov and Z.S. Wang, *Long-lived heavy neutral leptons at the LHC: four-fermion single- N_R operators*, *JHEP* **01** (2022) 044 [[2110.15096](#)].
- [41] R. Beltrán, G. Cottin, M. Hirsch, A. Titov and Z.S. Wang, *Reinterpretation of searches for long-lived particles from meson decays*, *JHEP* **05** (2023) 031 [[2302.03216](#)].
- [42] E. Fernández-Martínez, M. González-López, J. Hernández-García, M. Hostert and J. López-Pavón, *Effective portals to heavy neutral leptons*, *JHEP* **09** (2023) 001 [[2304.06772](#)].
- [43] D. Barducci, E. Bertuzzo, M. Taoso and C. Toni, *Probing right-handed neutrinos dipole operators*, *JHEP* **03** (2023) 239 [[2209.13469](#)].
- [44] W. Liu and Y. Zhang, *Testing neutrino dipole portal by long-lived particle detectors at the LHC*, *Eur. Phys. J. C* **83** (2023) 568 [[2302.02081](#)].
- [45] D. Barducci, W. Liu, A. Titov, Z.S. Wang and Y. Zhang, *Probing the dipole portal to heavy neutral leptons via meson decays at the high-luminosity LHC*, *Phys. Rev. D* **108** (2023) 115009 [[2308.16608](#)].
- [46] D. Barducci and A. Dondarini, *Neutrino dipole portal at a high energy μ -collider*, *JHEP* **10** (2024) 165 [[2404.09609](#)].
- [47] R. Beltrán, P.D. Bolton, F.F. Deppisch, C. Hati and M. Hirsch, *Probing heavy neutrino*

- magnetic moments at the LHC using long-lived particle searches, *JHEP* **07** (2024) 153 [2405.08877].
- [48] D. Barducci, E. Bertuzzo, M. Taoso, C.A. Ternes and C. Toni, *Illuminating the dark: mono- γ signals at NA62*, *JHEP* **10** (2024) 016 [2406.17599].
- [49] E. Bertuzzo and M. Frigerio, *Two portals to GeV sterile neutrinos : dipole versus mixing*, **2412.10101**.
- [50] L. Duarte, G. Zapata and O.A. Sampayo, *Final taus and initial state polarization signatures from effective interactions of Majorana neutrinos at future e^+e^- colliders*, *Eur. Phys. J. C* **79** (2019) 240 [1812.01154].
- [51] G. Zapata, T. Urruzola, O.A. Sampayo and L. Duarte, *Lepton collider probes for Majorana neutrino effective interactions*, *Eur. Phys. J. C* **82** (2022) 544 [2201.02480].
- [52] L. Duarte, G.A. González-Sprinberg and O.A. Sampayo, *Majorana neutrinos production at LHeC in an effective approach*, *Phys. Rev. D* **91** (2015) 053007 [1412.1433].
- [53] L. Duarte, G. Zapata and O.A. Sampayo, *Angular and polarization trails from effective interactions of Majorana neutrinos at the LHeC*, *Eur. Phys. J. C* **78** (2018) 352 [1802.07620].
- [54] G. Zapata, T. Urruzola, O.A. Sampayo and L. Duarte, *Sensitivity prospects for lepton-trijet signals in the ν SMEFT at the LHeC*, *Eur. Phys. J. C* **84** (2024) 326 [2305.16991].
- [55] M. Mitra, S. Mandal, R. Padhan, A. Sarkar and M. Spannowsky, *Reexamining right-handed neutrino EFTs up to dimension six*, *Phys. Rev. D* **106** (2022) 113008 [2210.12404].
- [56] L. Duarte, D.C. Maisian and T. Urruzola, *Future collider sensitivities to ν SMEFT interactions*, **2501.07618**.
- [57] J. Alcaide, S. Banerjee, M. Chala and A. Titov, *Probes of the Standard Model effective field theory extended with a right-handed neutrino*, *JHEP* **08** (2019) 031 [1905.11375].
- [58] H. Bahl, S. Koren and L.-T. Wang, *Topopportunities at the LHC: rare top decays with light singlets*, *Eur. Phys. J. C* **84** (2024) 1100 [2307.11154].
- [59] J.P. Chou, D. Curtin and H.J. Lubatti, *New Detectors to Explore the Lifetime Frontier*, *Phys. Lett. B* **767** (2017) 29 [1606.06298].
- [60] M. Bauer, O. Brandt, L. Lee and C. Ohm, *ANUBIS: Proposal to search for long-lived neutral particles in CERN service shafts*, **1909.13022**.
- [61] F. Garosi, D. Marzocca, A.R. Sánchez and A. Stanzione, *Indirect constraints on top quark operators from a global SMEFT analysis*, *JHEP* **12** (2023) 129 [2310.00047].
- [62] ATLAS collaboration, *Measurement of the $t\bar{t}$ production cross-section in the lepton+jets channel at $\sqrt{s} = 13$ TeV with the ATLAS experiment*, *Phys. Lett. B* **810** (2020) 135797 [2006.13076].
- [63] ATLAS collaboration, *Measurement of t -channel production of single top quarks and antiquarks in pp collisions at 13 TeV using the full ATLAS Run 2 data sample*, *JHEP* **05** (2024) 305 [2403.02126].
- [64] J. Alwall, M. Herquet, F. Maltoni, O. Mattelaer and T. Stelzer, *MadGraph 5 : Going Beyond*, *JHEP* **06** (2011) 128 [1106.0522].

- [65] J. Alwall, R. Frederix, S. Frixione, V. Hirschi, F. Maltoni, O. Mattelaer et al., *The automated computation of tree-level and next-to-leading order differential cross sections, and their matching to parton shower simulations*, *JHEP* **07** (2014) 079 [1405.0301].
- [66] M. Czakon and A. Mitov, *Top++: A Program for the Calculation of the Top-Pair Cross-Section at Hadron Colliders*, *Comput. Phys. Commun.* **185** (2014) 2930 [1112.5675].
- [67] K. Bondarenko, A. Boyarsky, D. Gorbunov and O. Ruchayskiy, *Phenomenology of GeV-scale Heavy Neutral Leptons*, *JHEP* **11** (2018) 032 [1805.08567].
- [68] T. Hahn, *Generating Feynman diagrams and amplitudes with FeynArts 3*, *Comput. Phys. Commun.* **140** (2001) 418 [hep-ph/0012260].
- [69] T. Hahn and M. Perez-Victoria, *Automatized one loop calculations in four-dimensions and D-dimensions*, *Comput. Phys. Commun.* **118** (1999) 153 [hep-ph/9807565].
- [70] ATLAS collaboration, *Search for long-lived, massive particles in events with displaced vertices and multiple jets in pp collisions at $\sqrt{s} = 13$ TeV with the ATLAS detector*, *JHEP* **06** (2023) 200 [2301.13866].
- [71] K. Cheung, F.-T. Chung, G. Cottin and Z.S. Wang, *Quark flavor violation and axion-like particles from top-quark decays at the LHC*, *JHEP* **07** (2024) 209 [2404.06126].
- [72] ATLAS collaboration, *Search for massive, long-lived particles using multitrack displaced vertices or displaced lepton pairs in pp collisions at $\sqrt{s} = 8$ TeV with the ATLAS detector*, *Phys. Rev. D* **92** (2015) 072004 [1504.05162].
- [73] N.D. Christensen and C. Duhr, *FeynRules - Feynman rules made easy*, *Comput. Phys. Commun.* **180** (2009) 1614 [0806.4194].
- [74] A. Alloul, N.D. Christensen, C. Degrande, C. Duhr and B. Fuks, *FeynRules 2.0 - A complete toolbox for tree-level phenomenology*, *Comput. Phys. Commun.* **185** (2014) 2250 [1310.1921].
- [75] NNPDF collaboration, *Parton distributions from high-precision collider data*, *Eur. Phys. J. C* **77** (2017) 663 [1706.00428].
- [76] P. Artoisenet, R. Frederix, O. Mattelaer and R. Rietkerk, *Automatic spin-entangled decays of heavy resonances in Monte Carlo simulations*, *JHEP* **03** (2013) 015 [1212.3460].
- [77] T. Sjöstrand, S. Ask, J.R. Christiansen, R. Corke, N. Desai, P. Ilten et al., *An introduction to PYTHIA 8.2*, *Comput. Phys. Commun.* **191** (2015) 159 [1410.3012].
- [78] M. Cacciari, G.P. Salam and G. Soyez, *FastJet User Manual*, *Eur. Phys. J. C* **72** (2012) 1896 [1111.6097].
- [79] CMS collaboration, *Enriching the Physics Program of the CMS Experiment via Data Scouting and Data Parking*, **2403.16134**.
- [80] CMS collaboration, *Search for long-lived heavy neutrinos in the decays of B mesons produced in proton-proton collisions at $\sqrt{s} = 13$ TeV*, *JHEP* **06** (2024) 183 [2403.04584].
- [81] ATLAS collaboration, *Commissioning of the ATLAS high-performance b-tagging algorithms in the 7 TeV collision data*, .
- [82] J.L. Feng, I. Galon, F. Kling and S. Trojanowski, *ForwArd Search ExpeRiment at the LHC*, *Phys. Rev. D* **97** (2018) 035001 [1708.09389].

- [83] FASER collaboration, *FASER’s physics reach for long-lived particles*, *Phys. Rev. D* **99** (2019) 095011 [[1811.12522](#)].
- [84] V.V. Gligorov, S. Knapen, M. Papucci and D.J. Robinson, *Searching for Long-lived Particles: A Compact Detector for Exotics at LHCb*, *Phys. Rev. D* **97** (2018) 015023 [[1708.09395](#)].
- [85] G. Aielli et al., *Expression of interest for the CODEX-b detector*, *Eur. Phys. J. C* **80** (2020) 1177 [[1911.00481](#)].
- [86] MATHUSLA collaboration, *An Update to the Letter of Intent for MATHUSLA: Search for Long-Lived Particles at the HL-LHC*, [2009.01693](#).
- [87] S. Cerci et al., *FACET: A new long-lived particle detector in the very forward region of the CMS experiment*, *JHEP* **06** (2022) 110 [[2201.00019](#)].
- [88] J.L. Pinfold, *The MoEDAL Experiment at the LHC—A Progress Report*, *Universe* **5** (2019) 47.
- [89] J.L. Pinfold, *The MoEDAL experiment: a new light on the high-energy frontier*, *Phil. Trans. Roy. Soc. Lond. A* **377** (2019) 20190382.
- [90] E. Etzion, “MATHUSLA: <https://indico.cern.ch/event/1381368/contributions/5963280/attachments/2887173/5061292/LLP2024-MATHUSLA-Etzion.pdf>.”, July, 2024.
- [91] L.D. Corpe, “Update on (pro)ANUBIS detector proposal: https://indico.cern.ch/event/1216822/contributions/5449255/attachments/2671754/4631593/LCORPE_LLWorkshop2023_ANUBIS_June2023.pdf.”, June, 2023.
- [92] J. Alwall et al., *A Standard format for Les Houches event files*, *Comput. Phys. Commun.* **176** (2007) 300 [[hep-ph/0609017](#)].